JOURNAL OF COMPUTATIONAL PHYSICS 66, 332–355 (1986)

Finite-Element Semi-Discretization of Linearized Compressible and Resistive MHD

W. KERNER, A. JAKOBY, AND K. LERBINGER

Max-Planck-Institut für Plasmaphysik, EURATOM Association
D-8046 Garching, Federal Republic of Germany

Received August 21, 1985; revised October 23, 1985

DEDICATED TO THE MEMORY OF RAYMOND C. GRIMM

The full resistive MHD equations are linearized around an equilibrium with cylindrical symmetry and solved numerically as an initial-value problem. The semi-discretization using cubic and quadratic finite elements for the spatial discretization and a fully implicit time advance yields very accurate results even for small values of the resistivity. In the application different phenomena such as waves, resistive instabilities, and overstable modes are addressed.

1. INTRODUCTION

A suitable description of the plasma behaviour is given by the macroscopic model (MHD). The existence of an MHD equilibrium is considered a necessary condition for successful operation of a tokamak. A large variety of instabilities can abruptly terminate the discharges or deteriorate their confinement. We regard resistive instabilities as the most important of the dissipative perturbations, since they cause the plasma to break away from the magnetic field. The ratio of the plasma pressure and the magnetic field energy, the plasma beta $\beta = 2p/\mathbf{B}^2$, should be as large as possible for economic reasons. The numerical search for stable equilibria, especially for optimized configurations, as well as for details of the instabilities is therefore very important for analyzing experiments and designing new devices. Complete simulation of the plasma evolution requires solution of the full time-dependent, nonlinear MHD equations. Owing to the quite different length and time scales involved this is a very complex numerical task.

Here we address the time evolution of linearized perturbations around an equilibrium state. Our numerical method is based on semi-discretization, where different approximations are used for the spatial and temporal discretization. In particular, the spatial discretization is chosen for good uniform numerical approximation of the entire spectrum of normal modes, a property that is not met by conventional schemes. It has been established that the linearized problem can be

0021-9991/86 $3.00

numerically solved with high accuracy. The influence of various quantities can thus be analyzed in detail; moreover, comparison with analytical theory [1, 2] is possible, which leads to fruitful interaction. The most common method of solving the linearized compressible, resistive MHD equations is the initial-value formulation. Hence this method has been used by many authors. We refer to the excellent review articles [3, 4, 5], which contain a detailed list of references. Explicit as well as implicit difference schemes have been employed for the time advance; see, for example, Ref. [6, 7].

In ideal MHD spectral codes using a sophisticated flux coordinate system and a finite-element discretization for the displacement vector, such as ERATO [8] and PEST [9], and also used by Kerner in Ref. [10], yield very accurate results, especially near the point of marginal stability. The formulation as an eigenvalue problem should therefore also be obvious for the set of resistive equations. In this respect the complex eigenvalues are evaluated by the matrix-shooting method of Freidberg and Hewett [11] or by the complex eigenvalue solver of Kerner, Lerbinger, and Steuerwald [12] using inverse vector iteration. Applications by Ryu and Grimm [13] utilizing the shooting method and by Kerner *et al.* [14, 15, 16] based on inverse vector iteration are so far all restricted to equilibria with cylindrical symmetry. A discretization using finite differences for the spatial variable can be made accurate to at least second order but requires a uniform mesh. To resolve resistive modes accurately, an extremely fine mesh around singular surfaces is necessary. The finite-element method allows arbitrary grid spacing, so that the mesh points can be appropriately accumulated around singular surfaces. This advantage easily makes up for the computational work needed to compute the matrix elements, which occur in the weak form. The Galerkin method in conjunction with cubic and quadratic finite elements was employed in the normal-mode code of Ref. [14]. A good discretization which approximates well the entire spectrum of normal modes was achieved there by representing the normal components of the velocity and the perturbed magnetic field by cubic Hermite elements, and the remaining components by quadratic finite elements. A pollution-free discretization (in the sense of Ref. [17, 18]) was thus obtained which yields very accurate results for the entire spectrum even for values of the resistivity as small as $\eta \approx 10^{-10}$, this was demonstrated in the applications of Ref. [12, 14, 15, 16]. Such a pollution-free discretization is extremely valuable at the marginal point. The entire spectrum can obviously be resolved only by a normal-mode code. An initial-value code always maps out the most unstable mode of the system. Therefore, it is unlikely that with the initial-value formulation a good discretization for the point of marginal stability has been obtained. Usually a finite-difference scheme requires much finer spatial resolution than a finite-element method with higher-order finite elements. The complex eigenvalues are obtained by means of a general eigenvalue problem $\mathscr{A}\mathbf{x} = \lambda\mathscr{B}\mathbf{x}$ with non-Hermitian matrix $\mathscr{A}$. The following complication then arises: If the matrix dimension is so large that iterative methods, such as inverse vector iteration, which preserve the band structure, become necessary, there is no guarantee against one or several eigenvalues being missed somewhere in the complex plane. Sylvester's

theorem (see Ref. [19]) of the Hermitian case valid for ideal MHD, which provides this information, does not apply to the dissipative system. To obtain such information, the Nyquist technique or a similar Cauchy integral becomes necessary, which is, however, rather involved. If we are concerned about missing the most unstable mode of a given configuration, we have to turn to the initial-value formulation. But, naturally, the good spatial discretization is kept. This concept of a finite-element discretization for the spatial dependence and the usual differencing in time is called semi-discretization.[1] This scheme perfectly complements the mentioned complex eigenvalue code. It should therefore be considered not as an extension of the normal-mode code but basically as a specific initial-value code.

The finite-element semi-discretization of the compressible, resistive MHD equations is the issue of this paper. For the time integration a fully implicit scheme is employed, which is unconditionally stable and thus allows arbitrarily large time-steps, this being extremely useful in the case of very small growth rates. All kinds of waves, such as fast and slow magnetoacoustic waves and Alfvén waves, can be accurately represented. If the time-step is too large for a specific wave such as the fast magnetosonic wave, this mode is not well represented but is damped out. The numerical scheme, however, still works accurately in representing slower modes such as Alfvén and sound waves. Current-driven tearing modes and pressure-driven resistive interchange modes are computed for different values of the resistivity. This demonstrates that our scheme indeed resolves resistive instabilities accurately and efficiently. Then overstable modes are analyzed, the growth rate and the oscillation frequency being resolved well for both large and small frequencies. The paper is organized as follows: The physical model, which is the common compressible, resistive MHD model, is described in Section 2. Details of the numerical scheme based on a finite-element semi-discretization are presented in Section 3, and its CPU times and storage requirements are discussed in Section 4. Section 5 contains the results: the capability of the code is demonstrated by the resolution of the various types of waves, by the treatment of resistive instabilities and by the application to overstable modes. Finally, Section 6 contains the discussion and the conclusions.

2. Physical Model

The plasma is described in terms of single-fluid theory. The resistive MHD equations read in normalized, dimensionless form

[1] Mechanics and Mathematical Methods, Computational Methods in Mechanics Vol. 1, Computational Methods For Transient Analysis, edited by T. Belytschko and Thomas J. R. Hughes (North-Holland, Amsterdam/New York/Oxford, 1983), Chap. 1 by T. Belytschko, "An Overview of Semidiscretisation and Time Integration Methods Procedures", Chap. 2 by Thomas J. R. Hughes "Analysis of Transient Algorithms with Particular Reference to Stability Behavior."

equation of motion

$$\rho\left(\frac{\partial \mathbf{v}}{\partial t}+\mathbf{v}\cdot\nabla\mathbf{v}\right)=-\nabla P+(\nabla\times\mathbf{B})\times\mathbf{B}, \tag{1}$$

Maxwell–Ohm

$$\frac{\partial \mathbf{B}}{\partial t}=\nabla\times(\mathbf{v}\times\mathbf{B})-\nabla\times(\eta\nabla\times\mathbf{B}), \tag{2}$$

adiabatic law

$$\frac{\partial P}{\partial t}=-\gamma P\nabla\cdot\mathbf{v}-\mathbf{v}\cdot\nabla P, \tag{3}$$

Maxwell

$$\nabla\cdot\mathbf{B}=0. \tag{4}$$

Here ρ denotes the density, $\mathbf{v}$ the velocity, $\mathbf{B}$ the magnetic field, P the pressure and η the resistivity; γ is the ratio of the specific heats. Note that the assumption of incompressibility, $\nabla\cdot\mathbf{v}=0$, is not made. The adiabatic law is adopted for the equation of state since the dissipation, which is proportional to η, is considered to be small. The incompressible equations of motion accurately describe the plasma behaviour if the pressure variations are small compared with the mean thermodynamic pressure. Since the resistive modes rapidly oscillate, the compressible set of equations is appropriate. The fast and slow magnetoacoustic waves are retained. These equations are now linearized around a static equilibrium characterized by $\partial/\partial t=0$ and $\mathbf{v}_0=\mathbf{0}$. The equilibrium is then determined by the equation

$$\nabla P_0=(\nabla\times\mathbf{B}_0)\times\mathbf{B}_0. \tag{5}$$

In straight geometry static, ideal equilibria can be interpreted as resistive equilibria if $\nabla\times\eta(\nabla\times\mathbf{B}_0)=0$, with the consequence that $\eta_0 j_0=E_z=\text{const}$. In toroidal geometry a resistive equilibrium is only possible with flow, i.e., $\mathbf{v}_0\neq\mathbf{0}$. This flow, however, is proportional to η and hence very small. Here we take the simplest approach of a constant resistivity η_0 instead of a constant E_z. This simplification does not constitute any restriction on unstable modes, since the resistivity decouples the fluid from the magnetic field in localized regions where the perturbation matches the field. But also the results for stable modes are only unsignificantly changed by using constant resistivity. This model thus gives the basic feature of resistive modes, since we are interested in phenomena which scale as $\eta^{3/5}$ or $\eta^{1/3}$ (and as $\eta^{1/2}$, like the resistive Alfvén modes). For a circular cylinder

the equilibrium quantities only have an r-dependence. With the usual cylindrical coordinates r, θ, z the equilibrium is determined by the equation

$$\frac{\partial P_0}{\partial r} = -\frac{1}{r} B_\theta \frac{\partial}{\partial r}(rB_\theta) - B_z \frac{\partial}{\partial r} B_z. \tag{6}$$

With two profiles given, Eq. (6) can be solved to give the remaining one.

The following separation ansatz is suitable for the perturbed quantities:

$$f(r, \theta, z; t) = f(r; t) \exp(im\theta + inkz). \tag{7a}$$

Introducing an eiganvalue

$$f(r; t) = f(r) \exp(\lambda t) \tag{7b}$$

then defines the growth rate as the real part of λ, i.e., $\lambda_R = \mathrm{Re}(\lambda)$. With $k = 2\pi/L$ defining a periodicity length, a tokamak with large aspect ratio is simulated, n corresponding to the toroidal mode number; m is the poloidal mode number. In ideal MHD λ is either real or purely imaginary, which leads to unstable or purely oscillating waves. With resistivity included, the frequency can become complex and hence overstable modes can occur. The equations for the perturbed quantities $\mathbf{v}$, p, and $\mathbf{b}$ read

$$\frac{\rho_0 \partial \mathbf{v}}{\partial t} = -\nabla p + (\nabla \times \mathbf{B}_0) \times \mathbf{b} + (\nabla \times \mathbf{b}) \times \mathbf{B}_0, \tag{8}$$

$$\frac{\partial p}{\partial t} = -\gamma P_0 \nabla \cdot \mathbf{v} - \mathbf{v} \cdot \nabla P_0, \tag{9}$$

$$\frac{\partial \mathbf{b}}{\partial t} = \nabla \times (\mathbf{v} \times \mathbf{B}_0) - \nabla \times (\eta \nabla \times \mathbf{b}). \tag{10}$$

The divergence condition, Eq. (4), for the perturbed field, $\nabla \cdot \mathbf{b} = 0$, is used to eliminate b_θ provided $m \neq 0$. The perturbed resistivity is set to zero, thus eliminating the rippling mode.

Finally, we discuss the boundary conditions. It is assumed that the plasma is surrounded by a perfectly conducting wall, which implies the following conditions at the wall,

$$v_r(a) = 0, \tag{11a}$$

$$b_r(a) = 0. \tag{11b}$$

For finite resistivity in the plasma the Maxwell equations require that the tangential component of the electric field vanish at the wall. This implies

$$\left(\frac{d}{dr} b_z\right)_{r=a} = 0. \tag{11c}$$

On the axis $r = 0$ all the quantities are regular.

3. Numerical Method

The system of linearized resistive MHD equations, Eqs. (8)–(10), presents a set of partial differential equations in the variables r and t. In semi-discretization methods these partial differential equations in space and time are first discretized in space yielding a system of ordinary differential equations in time. The semi-discretization in space can be accomplished by finite-element or finite-difference methods. Our formulation differs from the usual finite-difference schemes in that it imposes different requirements on the spatial and temporal discretization. The spatial discretization is tailored for a best (i.e., pollution-free) uniform approximation of the entire numerical spectrum to the exact spectrum. This was achieved by the special finite-element representation used in the normal-mode code of Kerner *et al.* [14]. The restriction on the temporal discretization is relatively mild. The method should be flexible to map out well all the different modes of the system with reasonable timesteps, which is easily obtained by an implicit method. The definition semi-discretization adopted by the authors (following footnote 1) underlines the different philosophy for the numerical approximation with respect to space and time. Approximation solutions are constructed by using the finite-element representation prompted by the complex eigenvalue code. The state vector $\mathbf{u}$ with six components is introduced:

$$\mathbf{u}'^{\mathrm{T}} = (v_r, v_\theta, v_z, p, b_r, b_z).$$

We then change the dependent variables to

$$\mathbf{u}^{\mathrm{T}} = (v_1 = rv_r, v_2 = iv_\theta, v_3 = irv_z, p' = rp, b_1 = irb_r, b_3 = rb_z). \tag{12}$$

For simplicity p' is named p again. To reduce the order of derivatives and to obtain the weak form, we take the inner product of Eqs. (8)–(10) with the weighting function $\mathbf{v}$, which has to be sufficiently smooth, and integrate over the plasma volume. In the Galerkin method used here the adjoint function $\mathbf{v}$ satisfies the same boundary conditions as $\mathbf{u}$. The operator in Eqs. (8)–(10) is represented by matrices $\mathscr{R}$ and $\mathscr{S}$ with spatial dependence only, where in $\mathscr{S}$ only the diagonal elements are

nonzero and $\mathscr{R}$ contains differential operators and equilibrium quantities. The set of equations then reads

$$\mathscr{R}\mathbf{u} = \mathscr{S}\frac{\partial \mathbf{u}}{\partial t}. \tag{13}$$

The components of $\mathbf{u}$ are approximated by a finite linear combination of local expansion functions or shape functions:

$$u^k = \sum_{j=1}^{2N} a_j^k(t)\, h_j^k(r), \qquad k = 1, 2, \ldots, 6 \tag{14}$$

with time dependence for the coefficients. Higher-order elements are used, namely cubic Hermite elements for the radial velocity and field components v_1 and b_1 and quadratic finite elements for v_2, v_3, p, and b_3. This introduces two orthogonal shape functions per interval, raising the order of the unknowns to $2N$, where $N-1$ denotes the number of radial intervals. With this choice the transverse divergence

$$\nabla_\perp \cdot \mathbf{v} = \frac{1}{r}\left(\frac{d}{dr} v_1 + m v_2\right) = 0 \tag{15}$$

can be made to vanish exactly in every interval, and the divergence of $\mathbf{b}$ as well. It has been established that this scheme yields a polution-free approximation for the discretized spectrum to the true eigenvalue spectrum. Condition (15), which is only a constraint for the numerical method, is the same as for the ideal system as shown in Ref. [14]. The proof that condition (15) is sufficient for uniform convergence to the exact spectrum in the ideal system has been given by Rappaz [18]. In the resistive case linear elements for v_1 and b_1 are not acceptable for a good discretization because of the higher-order derivatives in Ohm's law, and hence higher-order elements are required. The stated cubic and quadratic expansion functions were introduced in Ref. [14]. The vector $\mathbf{u}(r)$ is a weak solution if for any function $\mathbf{v}(r)$ of the admissible Sobolev space satisfying the boundary conditions the scalar product satisfies

$$(\mathscr{R}\mathbf{u}, \mathbf{v}) = \left(\mathscr{S}\frac{\partial \mathbf{u}}{\partial t}, \mathbf{v}\right).$$

In the Galerkin method, which is applied here, the basis functions $h_j^k(r)$ are used in the weak form, yielding

$$\mathscr{A}\mathbf{a} = \mathscr{B}\frac{\partial \mathbf{a}}{\partial t}, \tag{16}$$

where

$$A_{ij} = \int_{\Omega} R_{il} h_j^l(r)\, dr, \tag{17}$$

$$B_{ij} = \int_{\Omega} S_{il} h_j^l(r)\, dr, \tag{18}$$

are matrices of length $d = 12N - 2$, when the boundary conditions are taken into account. The integration is performed over the plasma volume Ω. The matrix $\mathscr{B}$ is symmetric and positive-definite but $\mathscr{A}$ is non-Hermitian. Equation (16) presents a system of linear ordinary differential equations. The simplest integration scheme for the first-order system (16) is the explicit Euler scheme

$$\mathbf{a}^{n+1} = \mathbf{a}^n + \Delta t\, \dot{\mathbf{a}}^n, \tag{19}$$

where n denotes the time-step, i.e., $t = t_0 + n\,\Delta t$. This yields the integration formula

$$\mathbf{a}^{n+1} = (\Delta t\, \mathscr{B}^{-1}\mathscr{A} + 1)\, \mathbf{a}^n. \tag{20}$$

This method is only conditionally stable (see footnote 1, Ref. [22]). Numerical stability limits the time step to

$$\Delta t \leqslant \frac{2}{\lambda_{\max}} = \Delta t_{\text{stab}}, \tag{21}$$

where $\lambda_{\max}$ is the maximum eigenvalue of the system $\mathscr{A}\mathbf{a} = \lambda\mathscr{B}\mathbf{a}$. Since the largest eigenvalue is given by the fast magnetosonic wave owing to the shortest radial scale Δr and hence tends to infinity if Δr goes to zero, the Courant–Friedrichs–Lewy (CFL) condition (21) is not acceptable. This CFL condition can be improved by adopting an implicit scheme defined by

$$\mathbf{a}^{n+1} = \mathbf{a}^n + \Delta t\, \dot{\mathbf{a}}^{n+1}, \tag{22}$$

which is unconditionally stable. We adopt the generalized trapezoidal method

$$\mathbf{a}^{n+1} = \mathbf{a}^n + \Delta t(1-\omega)\, \dot{\mathbf{a}}^n + \Delta t\, \omega \dot{\mathbf{a}}^{n+1}, \tag{23}$$

with parameter ω, which reduces to the explicit formula (19) for $\omega = 0$ and to the implicit formula (22) for $\omega = 1$. For $\omega = 0.5$ it is the standard trapezoidal rule. The algorithm for the time advance then assumes the form

$$\hat{\mathscr{A}}\mathbf{a}^{n+1} := \{-\mathscr{B} + \omega\, \Delta t\, \mathscr{A}\}\, \mathbf{a}^{n+1} = \hat{\mathscr{B}}\mathbf{a}^n := -\{\mathscr{B} + (1-\omega)\, \Delta t\, \mathscr{A}\}\, \mathbf{a}^n. \tag{24}$$

This time integration is conditionally stable for $\omega < 0.5$ with $\Delta t < 2/(1-2\omega)\, \lambda_{\max}$ and unconditionally stable for $\omega \geqslant 0.5$. The scheme is first-order accurate, except for $\omega = 0.5$, where it is second order. Thus it is desirable to set $\omega \geqslant 0.5$. The matrix

manipulations necessary for an implicit scheme usually present a serious problem both for the coding and for the efficiency of the algorithm. Sometimes the explicit scheme is preferred because of its simplicity, in spite of the CFL condition. For the linearized problem addressed here the matrix computation does not pose a severe problem, since the band structure of the matrices $\mathcal{A}$ and $\mathcal{B}$ is utilized in the algorithm. The matrices have block-diagonal structure with a band width of $b = 23$, resulting in an overall band width of 47. The operations necessary for solution of the linear system (24) are performed with routines from the LINPACK library. The

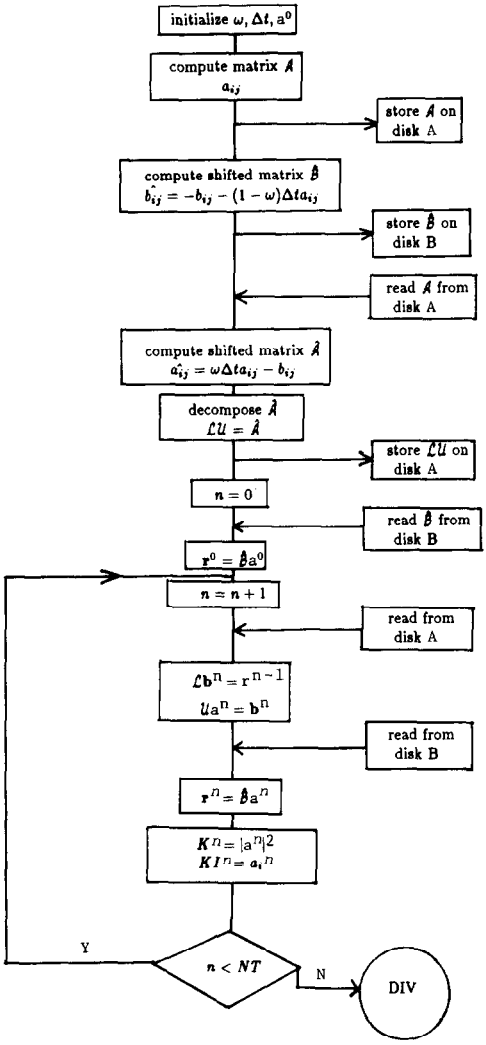

FIG. 1. Flow chart of the initial-value code based on semi-discretization with only one matrix in core.

elements outside the blocks but inside the band width are filled with zeros to be consistent with the required band-storage mode. The length of the matrices $d = 12 \cdot N - 2$ is usually large, namely $d \geqslant 1000$. The iterative system (24) is solved by applying $\mathscr{LU}$ decomposition of $\hat{\mathscr{A}}$. The algorithm is presented in the flow chart in Fig. 1. The temporal evolution of the initial vector $\mathbf{a}_0$ is monitored by the kinetic energy K to display the growth rate and by a specific component of $\mathbf{a}$ to display oscillations. Usually, the first component is chosen:

$$K(t) = \int dt\, |\mathbf{u}|^2 = \mathbf{a}^{\mathrm{T}} \mathscr{B} \mathbf{a} \to |\mathbf{a}|^2, \tag{25a}$$

$$K^n = |\mathbf{a}^n|^2, \tag{25b}$$

$$KI^n = a_i^n, \qquad 1 \leqslant i \leqslant d. \tag{25c}$$

By using the $\mathscr{LU}$ factorization the linear system (24) is solved very efficiently. The vector $\mathbf{a}$ is a real vector. The formulation as an eigenproblem (introduced by the ansatz (7b)) requires a complex vector $\mathbf{a}$ to represent imaginary and complex eigenvalues λ, and hence the algorithm for inverse vector iteration requires a complex shifted matrix $\mathscr{A}' = \mathscr{A} - \lambda_0 \mathscr{B}$. In comparison with the eigenvalue formulation this scheme is more economic with respect to storage. On the other hand, inverse vector iteration usually requires less iterations than the initial-value method.

4. Implementation

The implementation of the algorithm makes use of routines from the LINPACK library [21]. The real matrices $\mathscr{A}$ and $\mathscr{B}$ are evaluated and stored in the usual band-matrix storage mode, so that the zero elements outside the bands do not occur at all. Newt, the matrices $\hat{\mathscr{A}}$ and $\hat{\mathscr{B}}$ are computed according to Eq. (24) with the time-step Δt and the implicitness parameter ω fixed. To make full use of the fast execution on the CRAY-1 vector computer, the LINPACK routines SGBFA for factorization and SGBSL for successive solution of linear systems are used. The flow chart of the algorithm, presented in Fig. 1, displays the steps in the execution. The vector $\mathbf{a}_0$ is usually initialized by random numbers. Special choices prompted by analytical solutions or previous numerical results are admissible and can speed up the convergence. However, this is only done for convenience. The minimum amount of storage required includes the matrices $\mathscr{A}$ and $\mathscr{B}$ and the decomposition of $\hat{\mathscr{A}} = \mathscr{LU}$ together with the vectors $\mathbf{a}_i$ and $\mathbf{b}_i$. In addition, a workspace for the pivoting in the linear system has to be given. These storage requirements can easily be improved by keeping only the minimum data necessary for the algorithm in the fast memory and by storing data on disk. The storage-improved algorithm then works as follows:

(1) Compute matrix $\mathscr{A}$ and store $\mathscr{A}$ on disk, compute matrix $\mathscr{B}$ and perform the shift during computation $\hat{\mathscr{B}} = -\mathscr{B} - (1-\omega)\,\Delta t \mathscr{A}$ and store $\hat{\mathscr{B}}$ on disk B.

(2) Read in matrix $\mathscr{A}$ and perform the shift during computation $\hat{\mathscr{A}} = \omega\, \Delta t \mathscr{A} - \mathscr{B}$.

(3) Factor $\hat{\mathscr{A}} = \mathscr{L}\mathscr{U}$ and store $\mathscr{L}$ and $\mathscr{U}$ on disk A.

(4) Compute new vectors and keep $\mathbf{a}_i$ and $\mathbf{b}_i$ in the fast memory.

(5) Read in $\mathscr{L}$, $\mathscr{U}$, or $\hat{\mathscr{B}}$ separately, if needed.

This optimized version is a simple extension of the original one. Only one real matrix in band-matrix storage mode is required in the fast memory at any step together with additional workspace for the factorization with the dimension of the upper band width. The storage available at IPP, 7.3×10^6 bytes, which corresponds to 730,000 real words, allows 600,000 matrix elements together with the necessary vectors. Cases with up to 313 radial grid points resulting in a dimension d of the linear system of $d = 3742$ can be handled without storage on disk; this has been proved as sufficient for all the applications so far. A new solver utilizing the block-diagonal structure of the matrices and allowing a much larger block size is being tested and will be reported elsewhere. This new solver allows treatment of 2D equilibria.

Next we estimate the CPU time necessary for the algorithm. The number of operations to factor a band matrix with band width b and dimension d is

$$N_F \approx d \cdot b^2,$$

and the number of operations to solve the linear system

$$N_L \approx d \cdot b$$

For NT iterations there are then

$$N_I = N_F + NT \cdot N_L \approx d \cdot b(b + NT) \tag{26}$$

operations required. Usually, the number of time-steps is larger than 50 and, because b is fixed $b = 47$, the CPU time is approximately linear to both the number of time-steps NT and radial intervals N,

$$t(CPU) = aN(a' + NT) \approx aN \cdot NT, \tag{27}$$

with $a = 3.9 \times 10^{-4}$ and $a' = 69$. A typical case with 50 radial intervals and 500 time-steps then needs ~ 12.7 s on the CRAY-1. The additional vector and matrix manipulations, initially and at each time-step, together with the monitoring of $K(t)$ and $KI(t)$ slightly enhance the estimate (27).

5. Results

In this section three types of applications are presented, namely wave propagation, resistive current and pressure-driven instabilities, and overstable

modes. The semi-discretization in conjunction with the implicit time advance enables such phenomena to be accurately and efficiently resolved.

5.1. *Waves*

mode branches usually form a continuum. With resistivity point eigenvalues such as fast modes or ideal instabilities experience only a small change, mostly damping proportional to η, but the continua disappear and the resistive Alfvén modes are strongly damped (see Refs. [13, 15, 16]). Those eigenvalues lie on specific curves in the complex λ-plane which become independent of resistivity for vanishing η. If

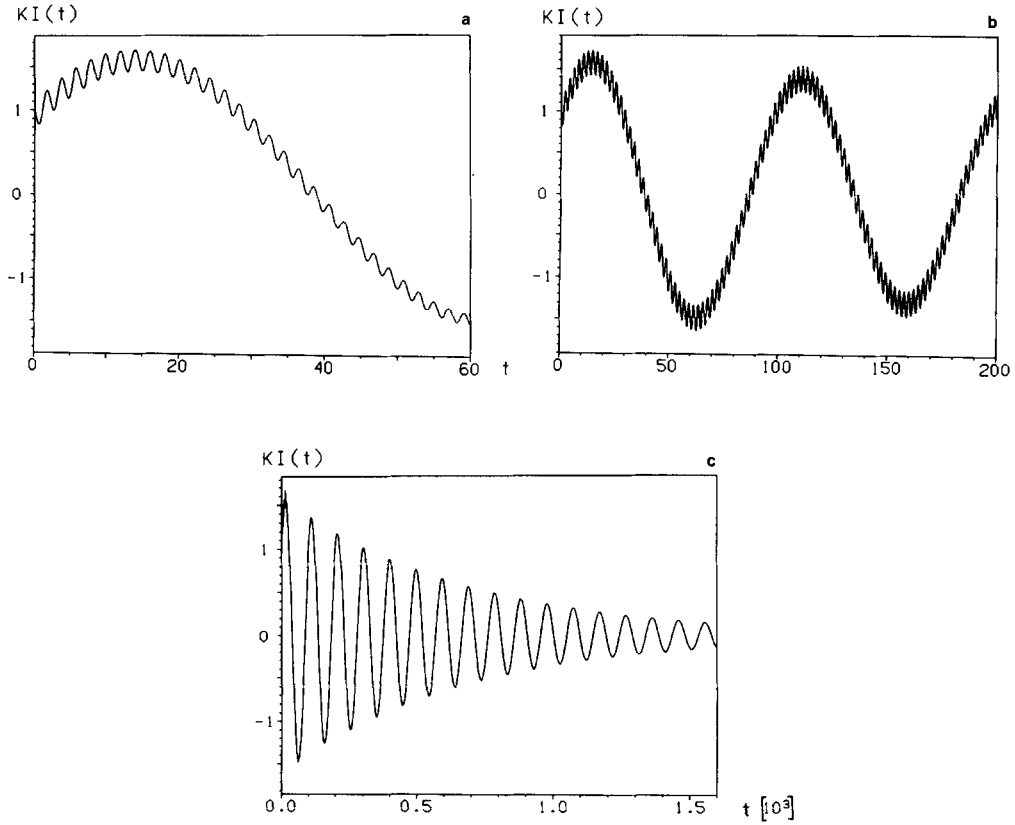

FIG. 2. Time evolution of a specific component of a fast magnetoacoustic wave superimposed on an Alfvén wave (KI, Eq. (25c). The rapid oscillations are due to the fast compressional wave with frequency $\mathrm{Im}(\lambda) = 3.06$ and with damping $\mathrm{Re}(\lambda) = -4.7 \times 10^{-6}$ and the slow decrease of $KI(t)$ is due to the Alfven wave with $\mathrm{Im}(\lambda) = 6.53 \times 10^{-2}$ and with $\mathrm{Re}(\lambda) = -1.36 \times 10^{-3}$. (a) $\omega = 0.52$ and $\Delta t = 0.075$, (b) $\omega = 0.50$ and $\Delta t = 0.25$, (c) $\omega = 0.52$ and $\Delta t = 2.0$.

initialized accordingly, the numerical scheme allows such waves to be analyzed. The equilibrium is the same as for the stability analysis below and is defined as

$$\begin{aligned} B_z(r) &= 1.0, \\ B_\theta(r) &= \frac{j_0}{4}(2r - r^3), \\ p(r) &= \frac{j_0}{4}\left((1-r^2) - \frac{3}{4}(1-r^4) + \frac{1}{6}(1-r^6)\right), \\ \rho_0(r) &= 1.0, \end{aligned} \tag{28}$$

where the constant j_0 is connected with the value of the safety factor on the axis $q(0)$ and the wave number k $j_0 = 2k/q(0)$. Figure 2 displays the time evolution of a fast mode superimposed on an Alfvén mode. The parameter ω is given two values $\omega = 0.52$ and 0.5. For a small time-step $\Delta t = 0.075$ the fast mode is properly resolved with the correct frequency $\mathrm{Im}(\lambda) = 3.06$ and with approximately the correct damping $\mathrm{Re}(\lambda) = -6.85 \times 10^{-6}$. Since the damping of the Alfvén mode is almost a factor of 1000 larger than that of the fast mode the correct damping $\mathrm{Re}(\lambda) = -4.7 \times 10^{-6}$ is obtained only with smaller time-steps or with the Alfvén wave switched off. The global decline of the amplitudes in Fig. 2a is due to the Alfvén wave, which is not followed for a long enough time. For larger time-steps $\Delta t = 0.25$ and $\Delta t = 2.0$ the Alfvén wave is better resolved; the corresponding frequency $\mathrm{Im}(\lambda) = 6.53 \cdot 10^{-2}$ and damping $\mathrm{Re}(\lambda) = 1.36 \times 10^{-3}$ have the correct values. For ω greater than 0.5 the fast modes are damped out but the numerical method is still stable and hence the Alfvén waves are properly resolved until the time step is eventually too large. For $\omega = 0.5$ the waves persist numerically undamped. These results confirm that the time-step is given by the accuracy necessary to resolve a specific mode, but not by stability. It is found that the time-step should be approximately equal to or smaller than 0.1 times the frequency, or the growth rate of the mode of interest.

5.2. *Resistive Instabilities*

The results so far have indicated that we are free to adjust the time-step for efficient resolution of any mode of the system. Next, current and pressure-driven resistive instabilities are analyzed. The results for a realistic tokamak-like equilibrium with peaked current density and constant toroidal fields is fairly well understood. The class of profiles

$$\begin{aligned} j_z(r) &= j_0\left(1 - \frac{r^2}{a^2}\right)^\nu, \\ B_z &= 1, \\ \rho &= 1 \end{aligned}$$

yields for the ratio of the safety factor on surface $r^{\text{surface}} = a$ and on axis $q(a)/q(0) = \nu + 1$. The constant j_0 is adjusted to vary $q(0)$. We set $\nu = 1$ and hence $q(a)/q(0) = 2$. Then the profiles used assume the form

$$B_\theta = j_0 r \frac{(2 - r^2)}{4}, \tag{29a}$$

$$p = \frac{j_0^2}{4}\left((1 - r^2) - \frac{3}{4}(1 - r^4) + \frac{1}{6}(1 - r^6)\right), \tag{29b}$$

where j_0 is connected with $q(0)$,

$$j_0 = \frac{2k}{q(0)}.$$

It is known that the $m = 1$ tearing mode is unstable if the $q = 1$ surface is inside the plasma. This instability can be avoided if $q > 1.0$ over the whole plasma radius. The $m = 2$ tearing mode is then the most dangerous instability. As expected for this monotonically decreasing pressure (see Ref. [22]), the unstable modes have purely exponential growth. The growth rate of the most unstable mode is plotted versus $q(a)$ in Fig. 3a. If the wall is placed directly at the surface $a = r^{\text{wall}}$, then the $m = 2$ tearing mode is unstable for $2.20 \leqslant q(a) \leqslant 4.0$. These results are obtained by studying the time evolution of a starting vector given by random initialization. The time-step is chosen as $\Delta t = 400$ for the strong instabilities near $nq(a) = 3$ and as $\Delta t = 1000$ for weaker instabilities around $nq(a) = 2.1$. For $nq(a) \leqslant 2.3$ the instability changes from a current-driven into a pressure-driven mode. This transition is displayed in Fig. 3b. The growth rates are extracted from the time dependence of the kinetic energy and from that of a specific component, introduced as $K(t)$ and $KI(t)$

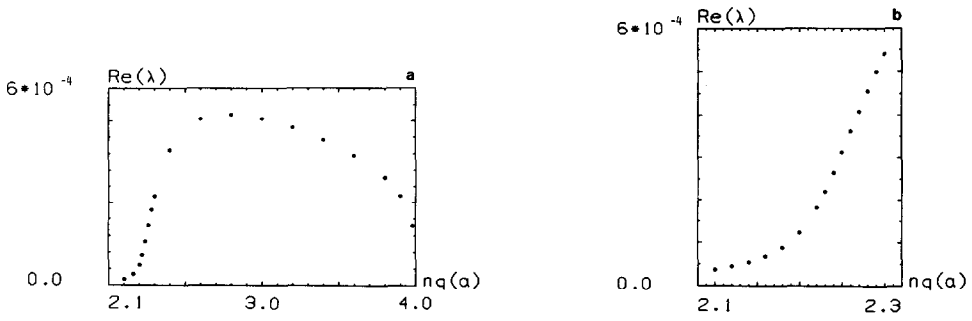

FIG. 3. (a) Growth rate of the most unstable mode for a tokmak-like current profile (Eq. (29)) with the wall directly at the plasma surface surface versus the safety factor on the surface for $\eta = 10^{-5}$ and $n = 1$, $m = -2$, $k = 0.1$, and $\omega = 0.52$. (b) Growth rate for the same case in an enlarged scale.

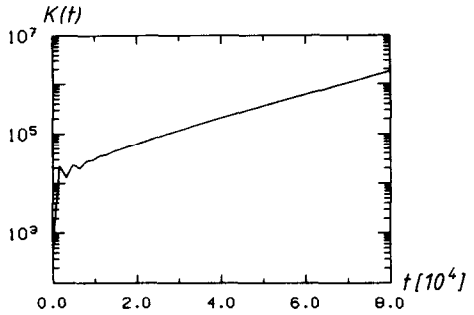

FIG. 4. Time evolution of the kinetic energy $K(t)$ of a pressure driven instability for the equilibrium of Fig. 3 with $q(a)=2.2$, $\omega=0.52$, and $\Delta t=400$.

in Eq. (25). Figure 4 shows the result for $nq(a)=2.2$. After a few initial oscillations a purely exponential growth for $K(t)$ is found. Note that only 50 to 100 time-steps are necessary to resolve such instabilities. This also holds for the scaling of a pressure-driven instability with resistivity. The smallest growth rate $\lambda_R \approx 10^{-6}$ for $\eta=10^{-9}$ is computed with a time step $\Delta t=2\cdot 10^5$. The expected dependence $\mathrm{Re}(\lambda)\sim\eta^{1/3}$ is found, as shown in Fig. 5. The eigenfunction displayed in Fig. 6 has a sharp gradient at the singular surface, which in this case is located at $r=0.95$ and is hence close to the wall. The perturbed pressure is significant for this instability in contrast to the purely current-driven tearing mode. To analyze these resistive instabilities thoroughly, the numerical accuracy has to be sufficiently high. This implies a fine spatial resolution around the singular surface. For a uniform radial grid the number of radial intervals has to be large to provide several points inside the resistive layer. Figure 7 displays the convergence study performed with a uniform mesh for the case of $nq(a)=2.2$, i.e., $r_s=0.95$. It is clearly seen that for a coarse grid such as $N=20$ or 40 the results are quite inaccurate. Furthermore, the growth rates oscillate with increasing number of intervals. This indicates that the location of grid points relative to the singular surface $r=r_s$ is more important than the number of points itself. Only for $N>60$ a reasonable convergence behaviour is evident. The dependence of $\mathrm{Re}(\lambda)$ on $1/N$ is then quartic up to $N=90$, where saturation is reached. If there is suitable mesh accumulation around the singular surface, con-

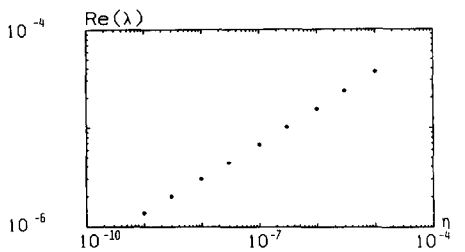

FIG. 5. Growth rate of the pressure driven instability for the tokamak-like equilibrium, Eq. (29), with $nq(a)=2.1$ versus resistivity for $n=1$, $m=-2$, and $k=0.1$.

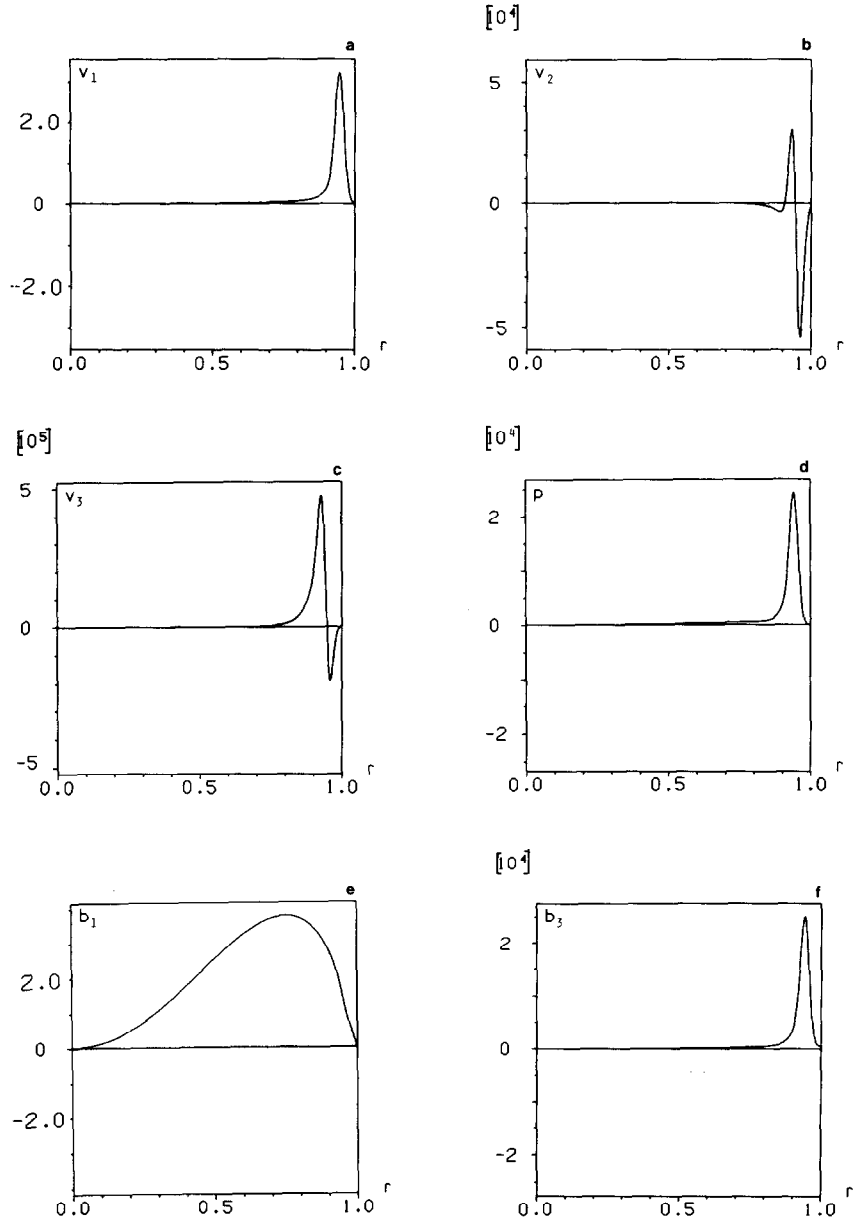

FIG. 6. Eigenfunction for the pressure driven instability for the equilibrium of Fig. 3 with $q(a) = 2.2$ and $\eta = 10^{-5}$.

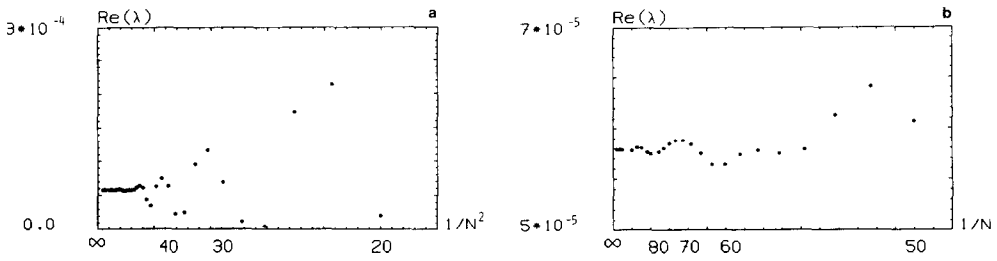

FIG. 7. Convergence study for the pressure driven instability for the tokamak-like equilibrium, Eq. (29), with $nq(a)=2.2$ ($r_a=0.95$), $n=1$, $m=-2$, $k=0.1$, and $\eta=10^{-6}$, the mesh is uniform, $\omega=0.52$, $\Delta t=400$ (a) in a quadratic scale for $N\geqslant 20$, (b) in a quartic scale for $N\geqslant 50$.

verged results are obtained with as few as $N\simeq 40$ points. Mesh accumulation was therefore built into the code. Then with a hundred radial mesh points a local resolution of $\Delta r/a=10^{-3}$ around $r=r_s$ can easily be generated. All results concerning instabilities presented in the paper are therefore computed by means of a non-uniform spatial grid and their convergence is checked by successive mesh refinement.

5.3. *Overstable Modes*

The linearized resistive MHD operator is non-selfadjoint, which leads to complex eigenvalues. The resistive fast magnetoacoustic and Alfvén waves experience both oscillatory behaviour and damping, as was demonstrated in the first application. To obtain an overstable mode in cylindrical geometry, the values for Δ', the jump of the logarithmic derivative of the perturbed magnetic field at the resonant surface, and for $D_S=-(2q^2/B_z^2q'^2)(dp/dr)$ have to be chosen accordingly. Overstable modes can occur only if $D_S<0$, which implies a locally increasing pressure, i.e., $dp/dr>0$, and if Δ' exceeds a critical value, $\Delta'>\Delta'_c$, as was pointed out in Ref. [22]. The class of tokamak-like equilibria defined by

$$\begin{aligned} B_z(r)&=\frac{1}{\alpha}\left(B_0^2-1+\left(\frac{1}{1+r^2}\right)^2\right)^{1/2},\\ B_\theta(r)&=\frac{1}{\alpha}\frac{r}{1+r^2},\\ p(r)&=\frac{1}{2}\frac{\alpha^2-1}{\alpha^2}\left(\frac{1}{1+r^2}-1\right),\\ \rho_0&=1 \end{aligned} \tag{30}$$

is suited to studying overstable modes (see Ref. [13]). The plasma extends up to the wall located at $r=r^{\text{wall}}=2.0$ For $\alpha=1$ we have a force-free configuration with zero pressure. For $\alpha<1$ finite pressure is introduced with $dp/dr>0$. Since the

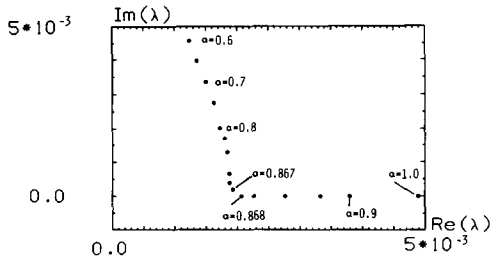

FIG. 8. Overstable modes for the tokamak-like equilibrium, Eq. (30), with varying pressure gradient. The values of α which labels dp/dr are given. The parameters are $B_0 = 9.0$, $\eta = 2 \times 10^{-5}$, $n = 1$, $m = -2$ and $k = 0.2$. Re(λ) denotes the growth rate and Im(λ) the oscillation frequency.

pressure is rising and nonzero at the wall, this equilibrium is somewhat unrealistic. But the pressure is quite small compared with the magnetic field pressure and therefore the model can be adopted for this study. The parameter B_0 labels the strength of the main field at the magnetic axis; it is used to adjust the value of the safety factor on axis. With $B_0 = 9.0$ and $k = 0.2$ we get $q(0) = 18$ and $q(a) = 89.47$. The singular surface with $q = 2$ is then $r_s = 0.34$. The value of D_S can be influenced directly by the parameter α. The value Δ' introduced in the analytic derivation is changed only indirectly by varying B_0 or η. The results are displayed in Fig. 8. In

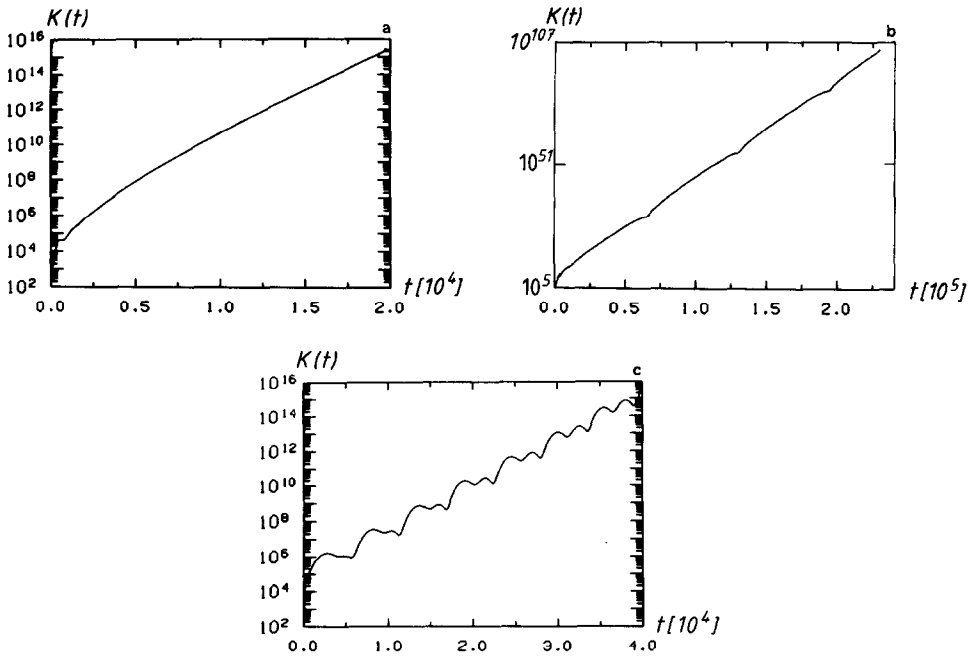

FIG. 9. Time evolution of the kinetic energy $K(t)$ of the instability for the tokamak-like equilibrium, Eq. (30); (a) $\alpha = 0.868$, Im(λ) = 0, (b) $\alpha = 0.867$, Im(λ) $\neq 0$, (c) $\alpha = 0.6$, Im(λ) $\neq 0$.

the force-free equilibrium ($\alpha = 1$) the only instability is the unstable tearing mode. If α gets smaller values, $\alpha < 1$, this mode becomes slightly stabilized, but a second unstable mode emerges from the origin. This second unstable mode is not detected by the initial-value code. With increasing pressure gradient, i.e., with decreasing values for α, the growth rate of the most unstable mode decreases and that of the second most unstable mode increases until both modes merge and an overstable mode evolves. This happens for $\alpha < 0.868$. If α is further decreased the growth rate of this overstable mode gets smaller. The oscillatory frequency, however, strongly increases. For $\alpha < 0.31$ the mode becomes stable with still finite oscillatory behaviour. The time evolution of the kinetic energy for a random initial vector shows no oscillatory behaviour for $0.868 \leqslant \alpha \leqslant 1$, as is seen from Fig. 9a. However, a small change to $\alpha = 0.867$ (Fig. 9b) indicates an oscillation, which becomes more pronounced for smaller values of α Fig. 9c. These plots allow the growth rate to be extracted with sufficient accuracy. The frequency of the oscillations, however, can be better extracted from the time evolution of a specific vector component $KI(t)$. To improve the resolution, we multiply $KI(t)$ by the factor $e^{-\lambda_R t}$ and thus prevent the amplitude from growing. As displayed in Fig. 10, we can then easily distinguish between purely growing modes with $\alpha = 1$ to $\alpha = 0.868$ (Fig. 10a,b) and oscillatory modes $\alpha < 0.868$ (Fig. 10c,d).

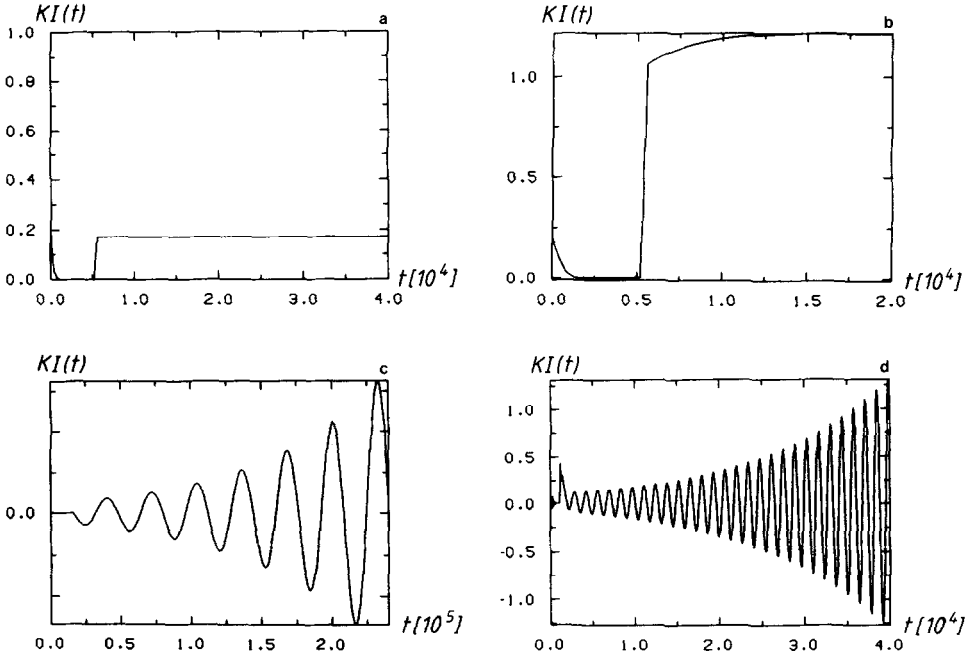

FIG. 10. Time evolution of a specific component of the eigenfunction $KI(t)$, modified by the factor $e^{-\lambda_R t}$, for the case of Fig. 9; (a) $\alpha = 1.0$, $\mathrm{Im}(\lambda) = 0$, (b) $\alpha = 0.868$, $\mathrm{Im}(\lambda) = 0$, (c) $\alpha = 0.867$, $\mathrm{Im}(\lambda) = 1.96 \cdot 10^{-4}$, (d) $\alpha = 0.60$, $\mathrm{Im}(\lambda) = 4.58 \cdot 10^{-3}$.

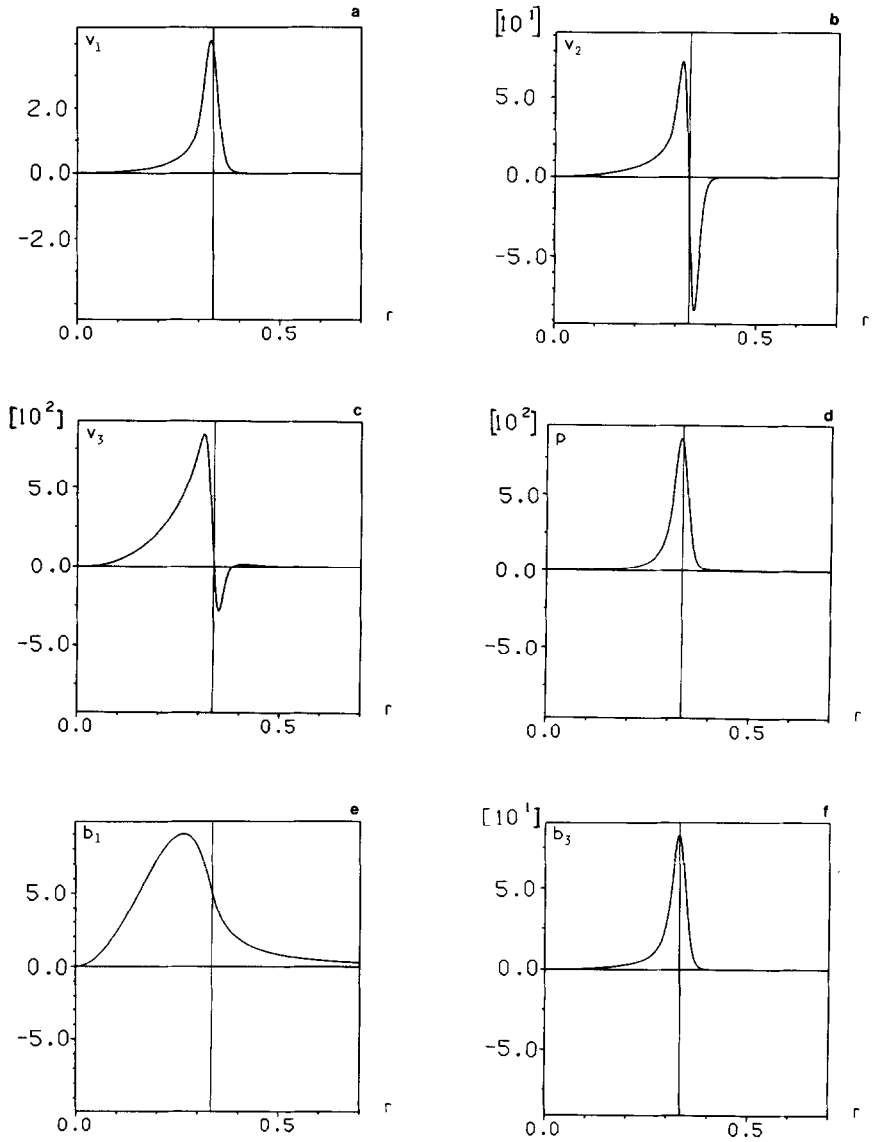

FIG. 11. Eigenfunctions of a purely growing instability for $\alpha = 0.868$ in Eq. (30). The singular surface at $r = r_s = 0.34$ is indicated.

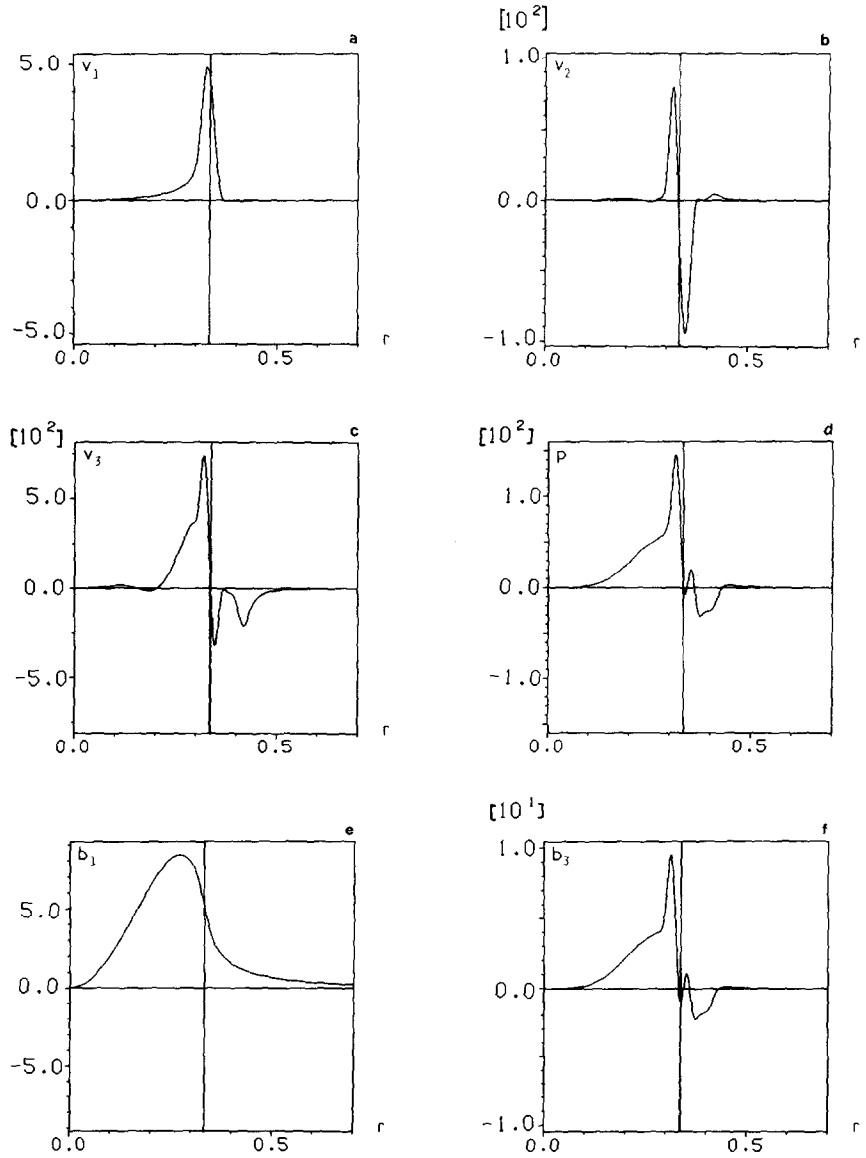

FIG. 12. Eigenfunctions of an overstable mode for $\alpha = 0.6$ in Eq. (30). The singular surface at $r = r_s = 0.34$ is indicated.

The exact value for the factor λ_R is not important here. Any approximate value will do. The modified quantity $KI(t)$ badly represents the initial part of the temporal evolution; but the distinction between purely growing behaviour, shown in Fig. 10a and b, and oscillatory behaviour, shown in Fig. 10c and d, is then extremely clear. Both the growth rate and the oscillation frequency can be determined with high accuracy. Relatively few time-steps are sufficient, i.e., $\Delta t = 20$ and $NT = 2000$ for $\alpha = 0.6$. If the constant α, which labels the pressure gradient, is decreased beyond values of 0.6, $\alpha < 0.6$, the accurate determination of the growth rate becomes more difficult. The frequency is still extracted; however, the time-step has to be substantially decreased. At $\alpha = 0.5$ the ratio of the growth rate and frequency becomes small $|\mathrm{Re}(\lambda)|/|\mathrm{Im}(\lambda)| \sim 10^{-3}/10^{-2} \approx 10^{-1}$. For reasonably accurate evaluation of the growth rate of such an overstable mode the time-step was set to $\Delta t = 1$, and many time-steps were necessary, $NT = 20{,}000$. The simulation of these instabilities becomes quite costly, since the CPU time rises by a factor of ten compared with the previous cases.

The difference between purely growing instabilities and overstable modes is now discussed. Figures 11 and 12 display the eigenfunctions for a purely growing mode $\alpha = 0.868$ and an overstable mode $\alpha = 0.6$. The first mode has the usual pattern of a tearing mode but here it has finite pressure. Note that the plasma extends from $r = 0$ to $r = r^{\mathrm{wall}} = 2.0$. The singular surface is located at $r = r_s = 0.34$. It is evident that the outer ideal part of the solution is not pronounced for $r > 0.5$ except for the radial perturbed field. The resolution in Figs. 11 and 12 is therefore increased by a cutoff for the radius at $v > 0.7$.

While the radial components of the velocity and magnetic field remain similar for both cases, the overstable mode has an additional structure in the other components. It is evident that the gradients directly at the singular surface $r = r_s$ become steeper and additional oscillations occur in the resistive layer. Especially, the perturbed pressure becomes more pronounced, which eventually leads to complete stabilization.

It was pointed out above that for such tokamak-like configurations the accuracy of overstable modes very strongly depends in a subtle manner on the equilibrium parameters. For slightly different parameters the effect is not there anymore. The detailed study of the modes presented therefore emphasizes the accuracy and reliability of the numerical scheme. In contrast to such a difficult case the overstable modes can very easily be traced for a reversed field pinch configuration, as presented by Ryu and Grimm [13].

6. Discussion

For understanding present fusion orientated experiments and for designing new devices numerical simulation is indispensable. The plasma behaviour can be understood in the context of nonlinear, resistive MHD theory. While the computation of equilibria and the linear ideal MHD stability analysis can be accurately

and efficiently solved, the long-time nonlinear simulation still presents a very hard problem. The corresponding initial-value codes have to resolve quite different temporal and spatial scales and easily exceed the computational resources. Completely implicit schemes together with appropriately moving coordinates appear necessary. These, however, are tremendously difficult to implement. Sophisticated and efficient methods are developed first in a linearized version, where plenty of test case exist both numerically and analytically. Good discretization can then be employed in the nonlinear codes.

The numerical method presented uses a different philosophy for the spatial and temporal discretization. The spatial discretization has to yield a pollution-free approximation for the entire spectrum of normal modes, this being obtained by a special finite-element representation. The requirement for the temporal discretization is simply given by stability and efficiency afforded by an implicit scheme. The resulting code differs substantially from all initial-value codes published. In the semi-discretization method presented the virtues of a finite-element normal-mode code and a fully implicit scheme are combined. The resistive layer is appropriately resolved with as few as fifty radial intervals, and large time-steps can be used, which allow one to extract the instabilities with fifty time-steps. This culminates in very accurate results which are very efficienctly computed. More than a hundred time-steps are needed just to determine the growth rate or the oscillatory frequency within error bars of less than one percent. Fast and slow magnetosonic and Alfvén

characterized by a very subtle dependence on equilibrium parameters are successfully treated. With the code presented, which is suited to monitoring linearized perturbations for cylindrical equilibria, obviously only the first step in the desired simulation of the temporal evolution of toroidal plasmas has been mastered. However, the semi-discretization used closes the gap between normal-mode and initial-value methods. The merits of the two schemes complement each other perfectly.

The next step in such a program consists in treating toroidal equilibria. This makes it necessary to introduce appropriate flux coordinates. This is the most obvious extension of the method presented.

Initial-value codes are made nonlinear with relative ease, since the distinction between equilibrium and perturbation is then discarded. The actual values of all quantities are updated at each time-step. However, magnetic islands develop, which makes the concept of adopted coordinates questionable. The introduction of higher-order two-dimensional finite elements thus appears to be desirable.

REFERENCES

1. H. P. FURTH, J. KILLEEN, AND M. N. ROSENBLUTH, *Phys. Fluids* **6**, 459 (1963).
2. B. COPPI, J. M. GREENE, AND J. L. JOHNSON, *Nucl. Fusion* **6**, 101 (1966).

3. K. V. ROBERTS AND D. E. POTTER, *Methods in Computational Physics*, edited by B. Alder (Academic Press, New York, 1970), Vol. 9, p. 340.
4. J. U. BRACKBILL, *Methods in Computational Physics*, edited by J. Killeen (Academic Press, New York, 1976), Vol. 16, p. 1.
5. D. SCHNACK AND J. KILLEEN, *J. Comput. Phys.* **35**, 110 (1980).
6. G. BATEMAN, W. SCHNEIDER, AND W. GROSSMAN, *Nucl. Fusion* **14**, 669 (1974).
7. J. A. DIBIASE AND J. K. KILLEEN, *J. Comput. Phys.* **24**, 158 (1977).
8. R. GRUBER, F. TROYON, D. BERGER, W. C. BERNARD, S. ROUSSET, R. SCHREIBER, W. KERNER, W. SCHNEIDER, AND R. V. ROBERTS, *Comput. Phys. Comm.* **21**, 323 (1981).
9. R. C. GRIMM, J. M. GREENE, AND J. L. JOHNSON, *Methods in Computational Physics*, edited by J. Killeen (Academic Press, New York, 1976), Vol. 16, p. 253.
10. W. KERNER, *Nucl. Fusion* **16**, 643 (1976).
11. J. P. FREIDBERG, D. W. HEWETT, *J. Plasma Phys.* **26**, 177 (1981).
12. W. KERNER, K. LERBINGER, J. STEUERWALD, *Comput. Phys. Comm. IPP* **6**, 236 (1984).
13. C. M. RYU AND R. C. GRIMM, *J. Plasma Phys.* **32**, 207 (1984).
14. W. KERNER, K. LERBINGER, R. GRUBER, AND T. TSUNEMATSU, *Comput. Phys. Comm.* **36**, 225 (1985).
15. W. KERNER AND K. LERBINGER, 1984 International Conference on Plasma Physics, Lausanne, Switzerland, June 27–July 3, 1984, paper P16-18.
16. W. KERNER, K. LERBINGER, K. RIEDEL, IPP 6/250, Max-Planck-Institut für Plasmaphysik Garching (1985); *Phys. Fluids*, in press.
17. K. APPERT, D. BERGER, R. GRUBER, AND J. RAPPAZ, *J. Comput. Phys.* **18**, 284 (1975).
18. J. RAPPAZ, *Numer. Math.* **28**, 15 (1975).
19. B. N. PARLETT, *The Symmetric Eigenvalue Problem* (Springer-Verlag, Berlin/Heidelberg/New York, 1971).
20. R. D. RICHTMEIER AND K. W. MORTON, *Difference Methods For Initial-Value Problems* (Interscience, New York/London/Sydney).
21. J. J. DONGERRA, C. B. MOLER, J. R. BUNCH, AND G. W. STEWART, *LINPACK User's Guide* SIAM, Philadelphia, 1979).
22. J. M. GREENE, École Polytechnique Fédérale de Lausanne, Centre de Recherches en Physique des Plasmas, Report LRP 114/76.